Semiclassical origin of the anomalous shell effect for tetrahedral deformation in the radial power-law potential model

Ken-ichiro Arita and Yasunori Mukumoto

Department of Physics, Nagoya Institute of Technology, Nagoya 466-8555, Japan

(Received 17 March 2014; published 8 May 2014)

Shell structures in single-particle energy spectra are investigated against regular tetrahedral type deformation using a radial power-law potential model. Employing a natural way of shape parametrization which interpolates sphere and regular tetrahedron, we find prominent shell effects for rather large tetrahedral deformations, which bring about shell energies much larger than the cases of spherical and quadrupole type shapes. We discuss the semiclassical origin of these anomalous shell structures using periodic orbit theory.

I. INTRODUCTION

Recent progress in experimental facilities has opened the new frontiers of unstable nuclei, where the combinations of neutron and proton numbers are considerably distant from the β stability line. Various kinds of exotic shapes are expected in several regions of deformed doubly magic nuclei as well as $N = Z$ regions (N and Z being neutron and proton numbers, respectively), where neutron and proton shell effects play cooperative roles. Tetrahedral deformed states are one of the candidates for such exotic states [1–3]. For such states, single-particle levels acquire degeneracies due to the high point-group symmetry of the Hamiltonian, and single-particle spectra show extra shell effects in comparison to the other types of deformations. Hamamoto *et al.* compared the four types of octupole deformations Y_{3m} ($m = 0, 1, 2$, and 3) in the modified oscillator model (Nilsson model without spin-orbit term), and found a stronger shell effect in Y_{32} shape, which possesses tetrahedral symmetry, in comparison to the other three [4]. They emphasized the occurrence of global level bunchings as well as the level degeneracies due to the point-group symmetry. In the analysis of electronic shell structures in sodium clusters with jellium model, notable shell effects were found for tetrahedral deformed states [5]. Interestingly, the resulting tetrahedral magic numbers, $N = 2, 8, 20, 40, 70, 112, \ldots$, are exactly the same as those for the spherical harmonic oscillator (HO) model. Dudek *et al.* investigated tetrahedral shell structures using the realistic nuclear mean-field model (including spin-orbit and Coulomb terms) with a more elaborate way of shape parametrization by adopting several combinations of spherical harmonics which are symmetric with respect to any transformation of a tetrahedral group [2]. They also found strong level bunchings for finite tetrahedral deformation. The deformed magic numbers are shifted from the HO values, which might be mainly due to the spin-orbit coupling. These level bunchings may suggest a restoration of dynamical symmetry by tetrahedral deformation, which are broken in a spherical potential with a sharp surface.

In Sec. II, we show the results of tetrahedral deformed shell structures using the radial power-law potential model, which we proposed as an approximation to the Woods-Saxon model [6,7]. One will see remarkable shell structures emerging in transition from spherical to regular tetrahedral

shapes. Semiclassical periodic orbit theory is applied to clarify the mechanism which brings about the above significant enhancement of shell effects. Semiclassical theory of shell structures are described in Sec. III. Special attention will be paid to the significance of periodic-orbit bifurcations. Trace formula for the radial power-law potential model is derived in Sec. IV. Properties of classical periodic orbits in the tetrahedral deformed potential are studied in Sec. V, and the quantum-classical correspondences are investigated in Sec. VI. Section VII is devoted for summary and discussions.

II. QUANTUM SHELL STRUCTURES IN TRANSITION FROM SPHERE TO TETRAHEDRON

If one parametrizes the tetrahedral type shapes only with a Y_{32} term, the shape becomes quite strange for large deformation, and classical dynamics turns strongly chaotic due to the negative curvature of the potential surface. Usually, one may not expect deformed shell structures to develop in such chaotic systems. In the present analysis, we make use of a simple and more natural way of shape parametrization which smoothly interpolates spherical and regular tetrahedral shapes with one parameter. We adopt the power-law type radial dependence of the potential, $V \propto r^\alpha$, which nicely approximates the Woods-Saxon type potentials inside the surface for systems with a wide range of constituent particle numbers [6,7]. This choice of the radial dependence is useful in both quantum and semiclassical analyses because of the scaling properties of the system [6–8].

The radial power-law potential model is described by the Hamiltonian

$$H = \frac{p^2}{2m} + U_0 \left(\frac{r}{R_0 f(\theta, \varphi; \beta_{\mathrm{td}})} \right)^\alpha. \tag{1}$$

Here, m is the mass of the constituent particles, U_0 and R_0 are the constants having dimensions of energy and length, respectively, which will be used as the units of those quantities. [U_0 is not an independent constant and we will fix it later: see Eq. (8) below.] $f(\theta, \varphi; \beta_{\mathrm{td}})$ is the tetrahedral shape function with deformation parameter β_{td}, given implicitly by the least positive root of the fourth order equation

$$f^2 + \frac{\beta_{\mathrm{td}}}{2} (1 + u_3(\theta, \varphi) f^3 - u_4(\theta, \varphi) f^4) = 1 \tag{2}$$
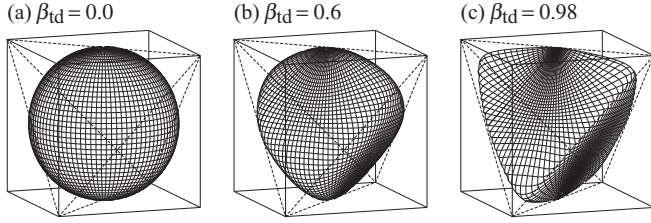
FIG. 1. Shapes of equipotential surface given by Eq. (2) with $\beta_{td} = 0$ (a), 0.6 (b), and 0.98 (c).

with

$$u_3(\theta, \varphi) = \tfrac{4}{15} P_{32}(\cos \theta) \sin 2\varphi, \tag{3}$$

$$u_4(\theta, \varphi) = \tfrac{1}{5} + \tfrac{4}{5} P_4(\cos \theta) + \tfrac{1}{210} P_{44}(\cos \theta) \cos 4\varphi . \tag{4}$$

u_3 and u_4 are symmetric under any transformation of the tetrahedral group $\boldsymbol{T}_d$. In Eq. (2), $\beta_{td} = 0$ corresponds to spherical shape ($f = 1$), and $\beta_{td} = 1$ corresponds to a regular tetrahedral shape (see Appendix A for the detailed derivation). Thus, one can smoothly change the shape of the potential from a sphere to regular tetrahedron, keeping the tetrahedral symmetry, by varying the single parameter β_{td} from 0 to 1. In order to satisfy the volume conservation condition, R_0 should be determined as a function of β_{td} by

$$R_0(\beta_{td}) = R_0(0) \left[\frac{1}{4\pi} \int d\Omega f^3(\Omega; \beta_{td}) \right]^{-1/3}. \tag{5}$$

Figure 1 shows the equipotential surface for several values of β_{td}. In our shape parametrization, the surface is convex everywhere for any value of β_{td}, and the classical orbits are less chaotic compared with the case of pure Y_{32} shapes

$$f(t_3) = 1 + t_3(Y_{32} + Y_{3-2}). \tag{6}$$

Actually, a pure Y_{32} equipotential surface shows concavity at $t_3 = 0.3$, a value where deformed shell effects are most enhanced, and it turns more eccentric for larger t_3.

The quantum spectra are calculated by diagonalizing the Hamiltonian with harmonic oscillator basis. After suitable scale transformations of variables, the Schrödinger equation for single-particle energy e is transformed into the following dimensionless form:

$$\left[-\frac{1}{2} \bar{\nabla}^2 + \left(\frac{\bar{r}}{f} \right)^\alpha \right] \psi(\bar{\mathbf{r}}) = \bar{e} \psi(\bar{\mathbf{r}}), \tag{7}$$

with

$$\bar{\mathbf{r}} = \frac{\mathbf{r}}{R_0}, \quad \bar{e} = \frac{e}{U_0}, \quad U_0 = \frac{\hbar^2}{m R_0^2}. \tag{8}$$

$\bar{\nabla}$ represents the derivative with respect to the dimensionless coordinate $\bar{\mathbf{r}}$. In the following part, we shall omit the bars on those variables and operators for simplicity. The diagonalization can be carried out in each block of irreducible representation (irrep) of $\boldsymbol{T}_d$ [9,10]. The group $\boldsymbol{T}_d$ has five irreps including three-dimensional representations. The f-dimensional irrep leads to the spectrum with f-fold degeneracy. In the diagonalization process, we can further decompose the bases into those of no degeneracy. A detailed
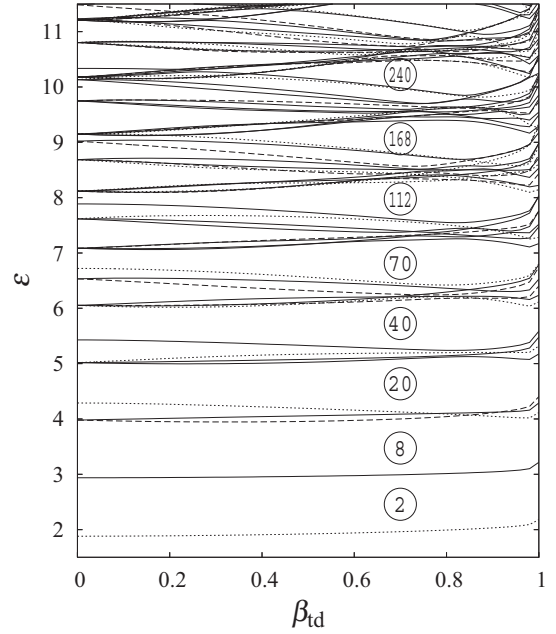

FIG. 2. Single-particle level diagram for radial parameter $\alpha = 6.0$. Scaled energy eigenvalues $\varepsilon_i = e_i^{1/2+1/\alpha}$ [see Eq. (26)] are plotted as functions of tetrahedral deformation parameter β_{td}. Dotted, dashed and solid curves represent levels belonging to irreps $A_{1,2}$, E and $F_{1,2}$, respectively. Circled numbers indicate magic numbers for the closed-shell configuration, taking the spin degeneracy factor into account.

procedure of the decomposition of bases making use of the $\boldsymbol{T}_d$ symmetry is presented in Appendix B.

For α close to 2, outstanding shell effects at the spherical shape (isotropic HO) are monotonically reduced by increasing tetrahedral deformation up to $\beta_{td} = 1$. For larger α, namely for potentials with sharper surfaces, spherical shell structures become moderate. However, we found the emergence of remarkable shell effects at rather large tetrahedral deformation. Figure 2 shows a single-particle level diagram for the case of radial parameter $\alpha = 6$, where quantum energy spectra are plotted against tetrahedral parameter β_{td}. One sees strong bunchings of levels and the appearance of large energy gaps around $\beta_{td} \approx 0.7$. The effect looks much more remarkable than those found in Refs. [2,4]. In order to compare the above tetrahedral deformation with the popular shape parametrization, let us expand our shape function $f(\beta_{td})$ by the spherical harmonics as in Eq. (6). One obtains the parameter t_3 by

$$t_3 = \int \frac{1}{2}(Y_{32} + Y_{3-2}) f(\beta_{td}) d\Omega. \tag{9}$$

For $\beta_{td} = 0.7$, we have $t_3 = 0.27$, which is close to the value for which tetrahedral shell effects are considerably enhanced in Ref. [2].

One will also note that the deformed magic numbers are exactly the same as those for the spherical harmonic oscillator, namely, $N = 2, 8, 20, 40, \ldots$, as obtained in Ref. [5]. These numbers are not changed by varying the value of parameter α in a range $\alpha \gtrsim 4$, while the deformation parameter β_{td} at

which the shell effect becomes most remarkable is shifted to a larger value as α increases.

The above situation also reminds us of the deformed shell structure in a two-dimensional billiard system where strong level bunchings are found in transition from circular to equilateral triangular shape [11]. The origin of this anomalous shell effect was understood as the bifurcation enhancement effect of short classical periodic orbits. This strongly encourages us to investigate the periodic orbits in our tetrahedral model and make a semiclassical analysis using periodic orbit theory.

III. SEMICLASSICAL THEORY OF SHELL STRUCTURES—THE ROLE OF THE PERIODIC ORBIT BIFURCATIONS

In semiclassical trace formula, the quantum energy level density $g(e)$ is expressed as the sum over contribution of classical periodic orbits [12]

$$g(e) = g_0(e) + \sum_k \sum_{n=1}^{\infty} g_{nk}(e), \qquad (10)$$

$$g_{nk}(e) = A_{nk}(e) \cos \left[\frac{n}{\hbar} S_k(e) - \frac{\pi}{2} \sigma_{nk} \right]. \qquad (11)$$

The sum in the right-hand side of Eq. (10) is taken over all primitive classical periodic orbits k and their nth repetitions. $S_k = \oint_k \mathbf{p} \cdot d\mathbf{r}$ is the action integral along the orbit k, σ_{nk} is the Maslov index for nth repetition of the orbit k which is an integer related with the geometric property of the orbit. For an isolated orbit, the amplitude factor $A_{nk}(e)$ is given by the Gutzwiller formula

$$A_{nk}(e) = \frac{N_k T_k}{\pi \hbar \sqrt{|\det(I - M_{nk})|}}, \qquad (12)$$

where T_k is the period of the primitive orbit k, and $M_{nk} = M_k{}^n$ is the monodromy matrix explained below. N_k is the multiplicity due to the discrete symmetry of the system, namely, there are N_k replicas of the orbit k generated by the symmetry transformations. $g_0(e)$ represents the average level density given by the Thomas-Fermi (TF) approximation [13],

$$g_{\mathrm{TF}}(e) = \frac{1}{(2\pi\hbar)^3} \int d\mathbf{p} d\mathbf{r} \delta(e - H(\mathbf{p},\mathbf{r})). \qquad (13)$$

The energy of the N particle system, $E(N)$, is decomposed into a smooth part and an oscillating part as [14]

$$E(N) = \tilde{E}(N) + \delta E(N), \qquad (14)$$

and the oscillating part, referred to as shell correction energy, is related with the oscillating part of the level density $\delta g(e)$ as [13,15]

$$\delta E(N) = \int_{-\infty}^{e_F} (e - e_F) \delta g(e) de, \qquad (15)$$

where e_F is the Fermi energy satisfying

$$\int_{-\infty}^{e_F} g(e) de = N. \qquad (16)$$

Inserting the semiclassical expression $\delta g(e) = \sum_{nk} g_{nk}(e)$, one obtains [13,15]

$$\delta E(N) = \sum_{nk} \left(\frac{\hbar}{n T_k(e_F)} \right)^2 g_{nk}(e_F). \qquad (17)$$

As seen from the above equation, longer periodic orbits have less contribution to the shell correction energy due to the factor $(nT_k)^{-2}$. Thus, the shell correction energy is dominated by the gross shell structure related with short periodic orbits.

In a three-dimensional system, calculations of classical periodic orbits require the search in a four-dimensional Poincaré section. The energy e defines a five-dimensional hypersurface in six-dimensional phase space. Let us define an appropriate four-dimensional hypersurface Σ in this five-dimensional energy surface. In the calculations below, we consider the hypersurface $\Sigma = \{Z \equiv (x,y,p_x,p_y)|z = 0, \dot{z} > 0\}$, p_z being determined by the energy condition $H(\mathbf{p},\mathbf{r}) = e$. Classical dynamics defines the mapping $\mathcal{M} : \Sigma \mapsto \Sigma$ (Poincaré map)

$$Z' = \mathcal{M}(Z), \quad Z, Z' \in \Sigma, \qquad (18)$$

where a classical orbit started at Z on Σ intersects Σ again later at Z'. The periodic orbits Z_k of period p are fixed points of the pth power of the Poincaré map,

$$Z_k = \mathcal{M}^p(Z_k), \qquad (19)$$

and the monodromy matrix M_k is the linearized Poincaré map around the periodic orbit

$$\delta Z'_k = \mathcal{M}^p(Z_k + \delta Z_k) - Z_k \simeq \left. \frac{\partial \mathcal{M}^p}{\partial Z} \right|_{Z_k} \delta Z_k \equiv M_k \delta Z_k. \qquad (20)$$

For nth repetitions, one has

$$\delta Z'_{nk} = M_k \delta Z'_{n-1,k} = \cdots = M_k{}^n \delta Z_k. \qquad (21)$$

Periodic orbit bifurcations occur when the monodromy matrix has unit eigenvalue, namely at $\det(I - M_k{}^n) = 0$. At the bifurcation deformation, the periodic orbit forms a local family of quasiperiodic orbits in the direction of the eigenvector belonging to the unit eigenvalue of the monodromy matrix. They make a coherent contribution to the level density and sometimes lead to a significant enhancement of the amplitude A_{nk}. This semiclassical mechanism nicely explains the enhancement of the deformed shell structure in many studies [16–20]. It also suggests a restoration of local dynamical symmetry, namely, the symmetry transformation generates a family of periodic orbits having the same periods and stabilities like, for instance, a degenerate family of orbits in rotationally symmetric potentials.

A substantial enhancement of the shell effect is expected in accordance with the so-called bridge orbit bifurcations. Typically, bridge orbits emerge between two quite different periodic orbits when their periods cross in the deformation-action $(\beta - S)$ plane [21]. For instance, consider the two-dimensional anisotropic harmonic oscillator (HO) perturbed by a nonlinear term. In a pure (unperturbed) HO system, there are two isolated diametric orbits along principal axes. When the two oscillator
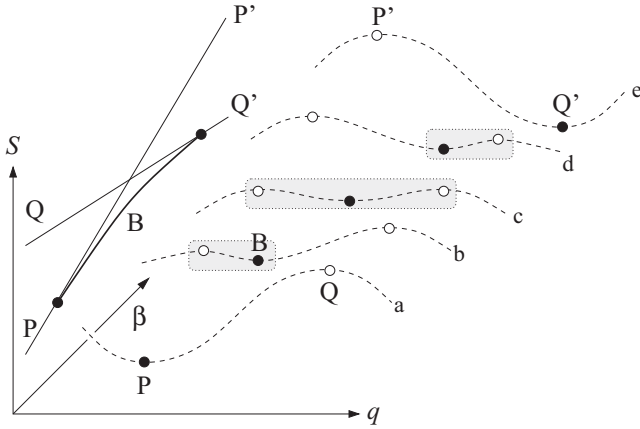
FIG. 3. Illustration of bridge orbit bifurcation scenario where orbit B bridges the two periodic orbits P and Q. Dashed curves represent the action integral $S(q)$ along the closed orbit for several values of deformation β. Its stationary points indicated by solid and open dots correspond to the stable and unstable periodic orbits, respectively. In the left-hand side, action integrals along those periodic orbits are shown by solid curves as functions of deformation β.

frequencies encounter in a rational ratio, all the classical orbits of Lissajous figures become periodic with same periods and stabilities, namely, they form a doubly degenerate family. This is related with the dynamical symmetry [22]. If a perturbation is imposed and the above dynamical symmetry is slightly broken, bridge orbits will replace the degenerate family, which emerge from one diameter at smaller deformation and then submerge into the other diameter at larger deformation. Since the loci or two diameters in phase space are quite distant from each other, bridge orbits will travel a long way in the phase space from one to the other during the bifurcation scenario. This is in contrast to usual bifurcations where all the participating periodic orbits reside in the vicinity of the central periodic orbit. Figure 3 illustrates an example of the bridge orbit bifurcation scenario. Action integral $S(q)$ along the closed orbit which starts q and returns to the same point q is shown as a function of q and deformation β. The stationary points indicated by solid and open circles correspond to periodic orbits. With increasing β, bridge orbit bifurcation occurs as follows:

(i) There are two periodic orbits P (stable) and Q (unstable).

(ii) The stable orbit P bifurcates and a new orbit B emerges. P turns unstable (P') afterwards. A local family of quasiperiodic orbits (indicated by the shaded range) are formed around orbits P and B.

(iii) Orbits P and Q cross in the $\beta_{td} - S$ plane. The quasiperiodic orbit family extends from P to Q.

(iv) Orbit B approaches the orbit Q.

(v) Orbit B submerges into the orbit Q, and Q becomes stable (Q') afterwards.

Thus, due to the coherent contribution of the quasiperiodic orbit family, the bridge orbit is expected to make a significant

contribution to the level density and leads to an enhancement of the shell effect. Since the family formed around the bridge orbit is extended between two orbits P and Q which are distant from each other in the phase space, this bifurcation is related with the restoration of a somewhat global dynamical symmetry in comparison to the simple bifurcations. Note that the bridge orbit does not appear for every crossing of two orbits in the $(\beta - S)$ plane. The appearance of bridge orbits might be an indication of the existence of global approximate dynamical symmetry.

IV. TRACE FORMULAS FOR THE RADIAL POWER-LAW POTENTIAL MODEL

Using the scaling invariance of our radial power-law potential model, the semiclassical analysis becomes quite simple. Since the Hamiltonian (1) has the scaling property

$$H(c^{1/2}\mathbf{p}, c^{1/\alpha}\mathbf{r}) = cH(\mathbf{p},\mathbf{r}), \tag{22}$$

the equations of motion are invariant under the scale transformation

$$\mathbf{p} \to c^{1/2}\mathbf{p}, \quad \mathbf{r} \to c^{1/\alpha}\mathbf{r}, \quad t \to c^{1/\alpha - 1/2}t,$$
$$\text{with} \quad e \to ce. \tag{23}$$

Therefore, classical dynamics does not depend on energy e, and classical trajectories at any energy e can be obtained from those at the certain reference energy e_0 by the scale transformation

$$(\mathbf{p}(t), \mathbf{r}(t))_e = (c^{1/2}\mathbf{p}(t'), c^{1/\alpha}\mathbf{r}(t'))_{e_0}$$
$$\text{with} \quad c = \frac{e}{e_0}, \quad t = c^{1/2 - 1/\alpha}t'. \tag{24}$$

Thus we have the same set of periodic orbits regardless of energy. The action integral along the periodic orbit k is written as

$$S_k(e) = \oint_{k(e)} \mathbf{p} \cdot d\mathbf{r} = \left(\frac{e}{e_0}\right)^{1/2 + 1/\alpha} \oint_{k(e_0)} \mathbf{p} \cdot d\mathbf{r} = \varepsilon\hbar\tau_k. \tag{25}$$

In the last equation, we define dimensionless *scaled energy* ε and *scaled period* τ_k;

$$\varepsilon \equiv (e/e_0)^{1/2 + 1/\alpha}, \quad \tau_k \equiv S_k(e_0)/\hbar, \tag{26}$$

which are proportional to the original energy e and period T_k, respectively, in the HO limit $\alpha \to 2$. Then, the semiclassical trace formula for the scaled-energy level density becomes

$$g(\varepsilon) = g(e)\frac{de}{d\varepsilon} \simeq g_0(\varepsilon) + \sum_{nk} a_{nk}(\varepsilon)\cos\left(n\varepsilon\tau_k - \frac{\pi}{2}\sigma_{nk}\right), \tag{27}$$

where amplitude factor $a_{nk}(\varepsilon)$ is related with the original one $A_{nk}(e)$ by

$$a_{nk}(\varepsilon) = \frac{de}{d\varepsilon}A_{nk}(e(\varepsilon)), \quad e(\varepsilon) = e_0\varepsilon^{\frac{2\alpha}{\alpha+2}}. \tag{28}$$

Using the Gutzwiller formula (12), the amplitude a_{nk} becomes

$$a_{nk} = \frac{N_k \tau_k}{\pi \sqrt{|\det(I - M_{nk})|}} \qquad (29)$$

which is independent of energy. The shell correction energy (17) becomes

$$\delta E(N) \simeq \frac{de}{d\varepsilon}\bigg|_{\varepsilon_F} \int^{\varepsilon_F} (\varepsilon - \varepsilon_F) \delta g(\varepsilon) d\varepsilon$$

$$= \frac{de}{d\varepsilon}\bigg|_{\varepsilon_F} \sum_{nk} \frac{1}{(n\tau_k)^2} a_{nk} \cos\left(n\tau_k \varepsilon_F - \frac{\pi}{2}\sigma_{nk}\right) \quad (30)$$

with

$$N = \int^{\varepsilon_F} \left(g_0(\varepsilon) + \sum_{nk} a_{nk} \cos\left(n\tau_k\varepsilon - \frac{\pi}{2}\sigma_{nk}\right)\right) d\varepsilon$$

$$= N_0(\varepsilon_F) + \sum_{nk} \frac{1}{n\tau_k} a_{nk} \sin\left(n\tau_k\varepsilon_F - \frac{\pi}{2}\sigma_{nk}\right). \quad (31)$$

$N_0(\varepsilon)$ is the average number of levels below the scaled energy ε. In the Thomas-Fermi approximation, g_0 and N_0 are given by

$$g_{\mathrm{TF}}(\varepsilon) = c_0 \varepsilon^2, \quad c_0 = \frac{2\sqrt{2}}{\pi} \mathrm{B}\left(1 + \frac{3}{\alpha}, \frac{3}{2}\right), \quad (32)$$

$$N_{\mathrm{TF}}(\varepsilon) = \int_0^\varepsilon g_{\mathrm{TF}}(\varepsilon') d\varepsilon' = \frac{c_0}{3}\varepsilon_F^3, \quad (33)$$

where $\mathrm{B}(s,t)$ is the Euler's beta function [7]. Note that $g_{\mathrm{TF}}(\varepsilon)$, and hence $N_{\mathrm{TF}}(\varepsilon)$, is independent of deformation under the volume-conservation condition. Since δE and N are both uniquely determined as functions of ε_F, one can obtain δE of N by using ε_F as the parameter.

V. CLASSICAL PERIODIC ORBITS

In order to estimate semiclassical level densities and shell correction energies by means of the trace formula, let us study the properties of short periodic orbits in a tetrahedral potential. In the spherical limit $\beta_{\mathrm{td}} = 0$ with $\alpha > 2$, there are two families of shortest orbits, diametric and circular ones, each of which are doubly degenerated. With increasing α, triply degenerated regular polygonal-type families of orbits bifurcate from the circular one. The first such family is the triangular type one which emerges at $\alpha = 7$. For $\alpha = 6$, the shortest orbits are only diameters and circles. Imposing the tetrahedral deformation, each of two families bifurcate into three kinds of isolated orbits. The diametric family bifurcates into diameter 'DA' along S_4 (fourfold rotatory reflection) axis, diameter 'DB' along C_3 (threefold rotation) axis, and librational 'PA' in the symmetry planes. These orbits have several replicas generated by the symmetry transformations. The multiplicities of DA, DB, and PA orbits are 3, 4, and 6, respectively. The circular family bifurcates into isosceles triangular type 'PB' in the symmetry plane, three-dimensional 'TA' having C_3 and σ_d (reflection) symmetries, and three-dimensional 'TB' having S_4 and σ_d symmetries. PB, TA, and TB orbits have multiplicities 12, 8, and 6, respectively. Those six kinds of orbits for $\alpha = 6$ and $\beta_{\mathrm{td}} = 0.3$ are illustrated in Figs. 4(a)–4(f). In each panel,
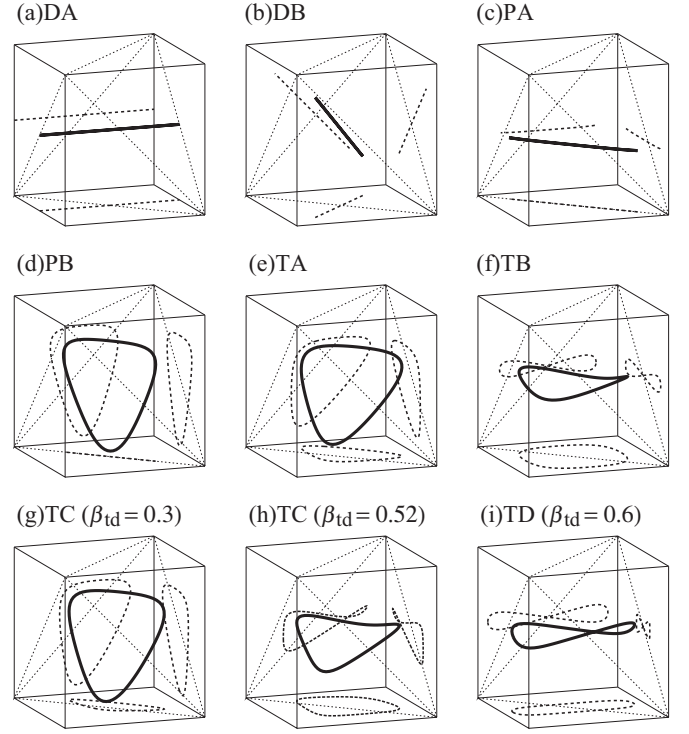

FIG. 4. Some short classical periodic orbits calculated for $\alpha = 6.0$. (a)–(f) are the six shortest orbits which exist at small β_{td}, drawn here for $\beta_{\mathrm{td}} = 0.3$. (g)–(i) are some bifurcated orbits for given β_{td}. In each panel, the thick solid curve represents the orbit and their projections onto the three faces of the outer cube are drawn with thick dashed curves. The tetrahedron drawn with dotted lines indicates the symmetry of the potential.

we also show the projections onto three faces of the outer cube and the tetrahedron expressing the symmetry of the potential for ease of understanding its geometry.

In Fig. 5, scaled periods τ_k of these shortest periodic orbits are plotted as functions of tetrahedral deformation parameter β_{td}. With increasing tetrahedral deformation, periods and stabilities of the orbits change and some of those orbits undergo bifurcations. The orbit PB undergoes bifurcation at $\beta_{\mathrm{td}} = 0.283$ and a three-dimensional orbit TC emerges from it. In this new orbit, all the symmetries are broken and its multiplicity is 24. With increasing β_{td}, it undergoes "touch-and-go" (nongeneric period-tripling) bifurcation [23] with the orbit TA at $\beta_{\mathrm{td}} = 0.369$ and finally submerges into the orbit TB at $\beta_{\mathrm{td}} = 0.600$. Namely, the orbit TC makes bridges between PB and TA, then between TA and TB. The orbit DA undergoes bifurcation at $\beta_{\mathrm{td}} = 0.562$ and three-dimensional orbit TD emerges from it. With increasing β_{td}, TD submerges into the orbit TB at $\beta_{\mathrm{td}} = 0.607$, namely, it makes a bridge between DA and TB. One should note that intensive bifurcations take place around $\beta_{\mathrm{td}} \sim 0.6$ and many of them form bridges between crossing periodic orbits in the region $\beta_{\mathrm{td}} = 0.6 \sim 0.8$. As discussed in the last part of Sec. III, the situation in our model, where periods of several periodic orbits come close to each other around $\beta_{\mathrm{td}} = 0.6$ and exchange bridge orbits between them, may indicate a global dynamical symmetry approximately restored in this deformation region.
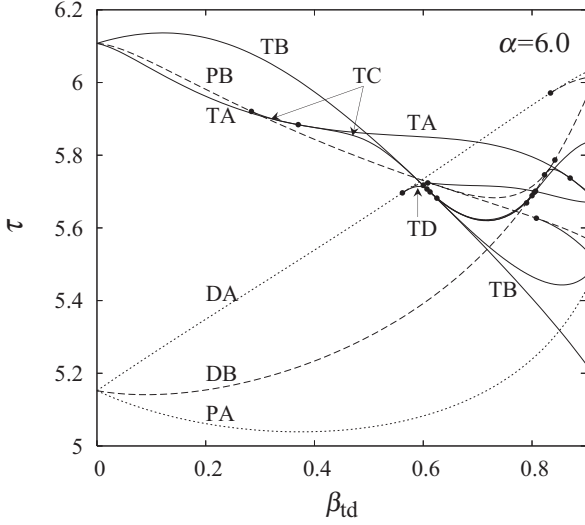
FIG. 5. Scaled periods of the shortest periodic orbits for $\alpha = 6$ as functions of the tetrahedral deformation parameter β_{td}. Solid, dashed, and dotted curves represent three-dimensional, planar, and diametric orbits, respectively. Solid circles indicate bifurcation points.

VI. SEMICLASSICAL ANALYSIS OF TETRAHEDRAL SHELL STRUCTURES

Knowing the classical periodic orbits in the previous section, let us proceed on to a semiclassical analysis of the deformed shell structures. In evaluating trace formula, periods, monodromy matrices, and Maslov indices are required. Periods and monodromy matrices are automatically obtained in the process of calculating periodic orbits by the monodromy method [24,25]. In order to calculate Maslov indices in a three-dimensional system, we devise a useful technique which is presented in Appendix C.

Figure 6 shows shell correction energies plotted as functions of the cubic root of particle number $N^{1/3}$ for $\alpha = 6.0$ with several values of β_{td}. Solid curves represent quantum mechanical results, and dashed curves represent the semiclassical results from Gutzwiller trace formula. For $\beta_{\mathrm{td}} = 0.1$, quantum shell correction energies show an obvious beating pattern, which is referred to as the supershell structure. In trace formula, the contribution of six orbits (DA, DB, PA, PB, TA, and TB) are taken into account. The above supershell structure is nicely reproduced as the result of interference between the contribution of shorter $\tau \simeq 5.2$ and longer $\tau \simeq 6.1$ periodic orbits. For $\beta_{\mathrm{td}} = 0.5$, we take account of the contribution of new orbit TC in addition to the above six orbits. Here, the shorter orbits PA and DB become strongly unstable and they do not have much contributions in the periodic orbit sum. Thus, since the dominating four orbits have similar periods here, the resulting shell structure shows somewhat simple oscillations. This also nicely reproduces the quantum result, where the supershell structure has disappeared. For $\beta_{\mathrm{td}} = 0.7$, The quantum shell energies show a regular and very strong shell effect. Here, the Gutzwiller formula breaks down due
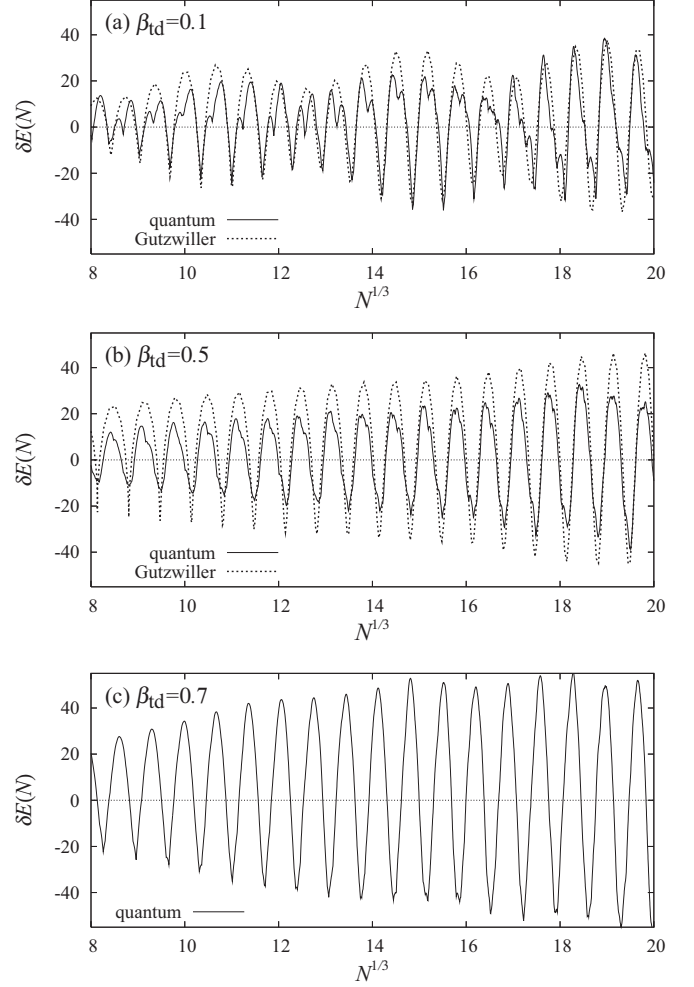

FIG. 6. Shell correction energies plotted as functions of the cubic root of particle number N for tetrahedral deformation parameters $\beta_{\mathrm{td}} = 0.1$ (a), 0.5 (b), and 0.7 (c), with radial parameter $\alpha = 6.0$. The solid curves represent quantum results, and the dotted curves represent semiclassical results from the Gutzwiller trace formula with shortest periodic orbits shown in Fig. 4.

to the occurrence of many bifurcations, but the remarkable enhancement of the shell effect here should be originated from coherent contributions of many bridge orbits having approximately the same periods.

In order to confirm the above scenarios, let us consider the Fourier transform of the scaled-energy level density

$$F(\tau) = \int e^{i\varepsilon\tau} g(\varepsilon) e^{-\frac{1}{2}(\varepsilon/\varepsilon_c)^2} d\varepsilon. \qquad (34)$$

The gaussian with cut-off energy ε_c is included in the integrand to suppress the contribution of level density at high energy ($\varepsilon \gg \varepsilon_c$) which is numerically unavailable. This function can be easily evaluated with the quantum mechanically obtained energy spectra $\{\varepsilon_i\}$ as

$$F^{(\mathrm{qm})}(\tau) = \sum_i e^{i\varepsilon_i\tau - \frac{1}{2}(\varepsilon_i/\varepsilon_c)^2}. \qquad (35)$$
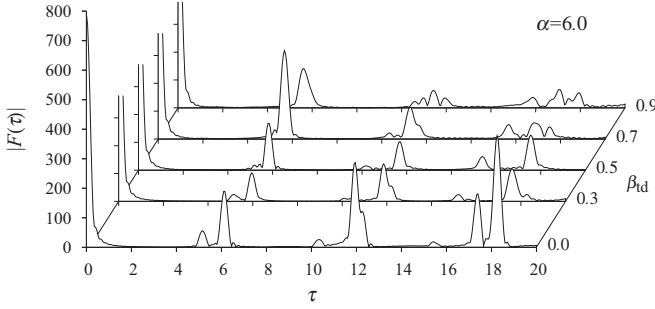
FIG. 7. Moduli of Fourier transform of quantum level density for $\alpha = 6.0$ with several values of β_{td}.

On the other hand, a substitution of semiclassical formula (27) into Eq. (34) gives

$$F^{(cl)}(\tau) \simeq F_0(\tau) + \pi \sum_{nk} e^{-i\frac{\pi}{2}\sigma_{nk}} a_{nk} \delta_\Delta(\tau - n\tau_k), \qquad (36)$$

where $\delta_\Delta(x)$ represents the normalized gaussian with the width $\Delta = 1/\varepsilon_c$:

$$\delta_\Delta(x) = \frac{1}{\sqrt{2\pi}\,\Delta} e^{-\frac{1}{2}(x/\Delta)^2}.$$

Thus, the Fourier transform of level density should exhibit peaks at the scaled periods $\tau = n\tau_k$ of classical periodic orbits k (and their repetitions) with the peak heights proportional to the amplitude factor a_{nk} of the corresponding orbits.

Figure 7 shows the Fourier amplitude of the quantum level density for $\alpha = 6.0$ with several values of β_{td}, plotted as functions of τ. At spherical shape ($\beta_{td} = 0$), one finds peaks at $\tau \simeq 5.1$ and 6.1, which correspond to linear and circular periodic orbits, respectively. At small β_{td}, these two contributions interfere and build the supershell structure as shown in Fig. 6(a). One also finds big peaks at larger τ; for example, the peak at $\tau \simeq 12$ corresponds to a five-star orbit bifurcated from the second repetition of the circular orbit. These longer orbits contribute to the finer shell structures and do not affect the shell correction energy much. Therefore, let us focus on the two peaks of small τ. In increasing tetrahedral parameter β_{td}, the left peak corresponding to the diametric orbits rapidly decreases, while the right peak significantly increases and take maximum value around $\beta_{td} = 0.7$. It is now clear from this peak structure that the supershell structure disappears and turns into regular oscillations as β_{td} increases, and the shell effect is strongly enhanced around $\beta_{td} \approx 0.7$ where periods of many periodic orbits gather into approximately the same value. This clearly explains the behavior of the single-particle level structure in Fig. 2 and of the shell correction energies in Fig. 6.

Figure 8 shows the correspondence between the Fourier transform of the quantum level density and classical periodic orbits. One will see nice agreements between the peaks of Fourier amplitudes and classical periodic orbits. One should also notice that the Fourier peak is strongly enhanced in the bifurcation region $\beta_{td} = 0.6 \sim 0.8$. Thus we can conclude that the anomalous shell effect emerging at large tetrahedral deformation originates from the quasidegeneracies of the
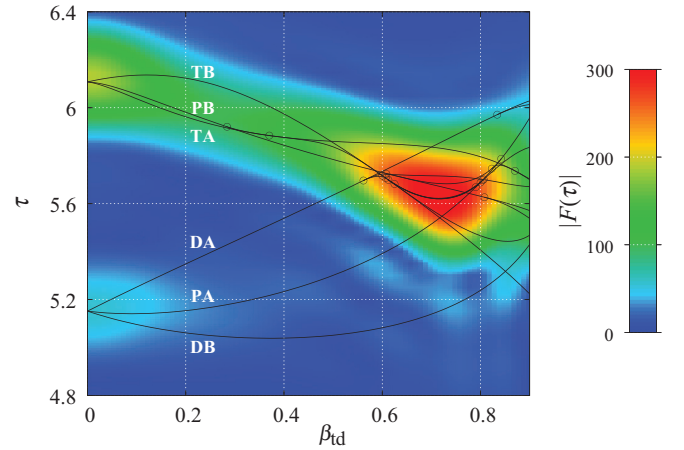

FIG. 8. (Color online) Quantum-classical correspondence in Fourier spectra. Quantum Fourier amplitudes $|F(\tau; \beta_{td})|$ are shown by the color. Solid curves represent the scaled periods of classical periodic orbits as functions of β_{td}, and solid circles indicate bifurcation points.

periods of several periodic orbits and the multiple bridge bifurcations among them, which may be related to the restoration of dynamical symmetry as discussed in previous sections.

VII. SUMMARY AND DISCUSSIONS

Novel shell structures developed by the tetrahedral deformation have been investigated. We have shown that this anomalously strong enhancement of shell effects in the nonintegral system has a close relation to the bridge bifurcations of periodic orbits having almost the same periods, which are similar to the situation in a rational HO system. Its relation to the fact that the tetrahedral magic numbers are exactly the same as those for spherical HO might also be an interesting problem.

In evaluating the semiclassical level density, the Gutzwiller formula overestimates the amplitude factor and we could not reproduce the shell structures in the bifurcation region, which we are most interested in. One of the ways to overcome this problem will be the use of uniform approximations [26]. One may suspect that the bifurcations in three-dimensional systems might be quite complicated in comparison to the two-dimensional case where all the basic bifurcation scenarios are classified by catastrophe theory [23]. Fortunately, we can expect that most of the bifurcations might be analyzed in the same way as in two-dimensional systems. Since the monodromy matrix has a unit eigenvalue at the bifurcation point, four eigenvalues of the monodromy matrix of bifurcating orbits must be decomposed into two conjugate/reciprocal pairs. Thus, we can reduce the dimension by decomposing the phase space into those spanned by eigenvectors belonging to each pair of eigenvalues. A practical procedure might be complicated, but it is of great interest to us to estimate semiclassical level densities and shell correction energies in the bifurcation regions and reproduce the anomalous shell effect obtained for the tetrahedral state.

For more quantitative discussions on nuclear systems, one should take account of the spin-orbit coupling. It is also an important subject to examine if the strong shell effect obtained in this work might survive after introducing the appropriate spin-orbit coupling, and how the resulting shell structures might be explained in periodic orbit theory.

APPENDIX A: TETRAHEDRAL SHAPE PARAMETRIZATION

Let us consider the tetrahedron whose four vertices are located at $(-R_0, -R_0, -R_0)$, $(-R_0, R_0, R_0)$, $(R_0, -R_0, R_0)$, and $(R_0, R_0, -R_0)$. The equations of four faces are

$$x + y + z = R_0, \quad x - y - z = R_0,$$
$$y - z - x = R_0, \quad z - x - y = R_0. \tag{A1}$$

On the surface of the tetrahedron, one of the above four equations is satisfied, namely,

$$(R_0 - x - y - z)(R_0 - x + y + z)(R_0 - y + z + x)$$
$$\times (R_0 - z + x + y) = 0. \tag{A2}$$

It is transformed into spherical coordinates (r, θ, φ) as

$$R_0^4 - 2R_0^2 r^2 - R_0 u_3(\theta, \varphi)r^3 + u_4(\theta, \varphi)r^4 = 0 \tag{A3}$$

with

$$u_3(\theta, \varphi) = \tfrac{4}{15} P_{32}(\cos \theta) \sin 2\varphi, \tag{A4}$$

$$u_4(\theta, \varphi) = \tfrac{1}{5} + \tfrac{4}{5} P_4(\cos \theta) + \tfrac{1}{210} P_{44}(\cos \theta) \cos 4\varphi, \tag{A5}$$

where $P_l(x)$ and $P_{lm}(x)$ are the Legendre polynomial and associated Legendre function, respectively. The functions u_3 and u_4 are both symmetric under the transformations of the tetrahedral group. The equation of tetrahedral surface can be obtained as the least positive root of the above fourth-order equation of r. Writing $r = R_0 f(\theta, \varphi)$, this equation becomes

$$1 - 2f^2 - u_3 f^3 + u_4 f^4 = 0. \tag{A6}$$

If one introduces a parameter β_{td} and modifies the above equation as

$$f^2 + \frac{\beta_{\mathrm{td}}}{2}(1 + u_3 f^3 - u_4 f^4) = 1, \tag{A7}$$

$\beta_{\mathrm{td}} = 0$ gives the sphere ($f = 1$), and $\beta_{\mathrm{td}} = 1$ gives the equation identical to Eq. (A6), namely, the tetrahedron. Thus, by varying the parameter β_{td} from 0 to 1, one can smoothly interpolate the sphere and tetrahedron keeping the tetrahedral symmetry.

APPENDIX B: IRREPS OF TETRAHEDRAL GROUP AND THE BASIS DECOMPOSITION PROCEDURE

The tetrahedral group T_d contains 24 symmetry transformations which are classified into five classes: identity E, eight rotations C_3, six rotatory reflections S_4, three rotations C_2, and six reflections σ_d. Here we follow the notations in Ref. [9]. This group has five irreducible representations (irreps): two one-dimensional irreps A_1, A_2, one two-dimensional irrep E, and two three-dimensional irreps F_2, F_1. The quantum spectra can be obtained by a diagonalization of the Hamiltonian within the bases of each irrep. After the complete decomposition of the bases, the dimensions of the Hamiltonian matrix for irreps A, E, and F are about 1/24, 1/12, and 1/8, respectively, of the total number of bases. Thus one can highly reduce the numerical loads by the basis decomposition.

For the construction of the basis, the irreps of the rotational group are employed. The basis function of the rotational group is given by spherical harmonics Y_{lm}. They form reducible representations of the group T_d, and the decomposition to each irrep can be carried out by the projection method [10]. The projection operator onto the irrep α is given by

$$P^{(\alpha)} = \frac{f_\alpha}{g} \sum_G \chi^{(\alpha)*}(G)G, \tag{B1}$$

where the sum is taken over all the symmetry transformations G of the group T_d, $g = 24$ is the order of the group T_d, f_α is the dimension of the irrep α, and $\chi^{(\alpha)}(G)$ is the character of G in the irrep α. By applying the $P^{(\alpha)}$ on Y_{lm}, a linear combination of the bases of irrep α included in Y_{lm} is extracted. GY_{lm} can be calculated by the Euler angle representation of the transformation G as

$$R(\Omega)Y_{lm} = \sum_{m'} D_{m'm}^{(l)}(\Omega)Y_{lm'}, \tag{B2}$$

where $R(\Omega)$ is the rotation with Euler angles Ω, and $D_{m'm}^{(l)}(\Omega)$ is the Wigner's D function. The complete set of the bases in irrep α are obtained by extracting all the linearly independent functions out of $2l + 1$ functions $P^{(\alpha)}Y_{lm}$ ($-l \leqslant m \leqslant l$) by the Gramm-Schmidt orthogonalization process.

The spectrum in irrep E is doubly degenerated and the bases can be further decomposed into two parts by the parity with respect to a reflection σ_d. The spectrum in irreps F are triply degenerated and the bases are also decomposed by σ_d into two parts: one is doubly degenerated and the other is of no degeneracies. In obtaining spectra, one has only to consider the nondegenerated part, which corresponds to $\sigma_d = -1$ for the irrep F_2 and $\sigma_d = 1$ for the irrep F_1.

In the current numerical calculations, we diagonalized the Hamiltonian using the spherical harmonic oscillator bases with 41 major shells ($0 \leqslant N_{\mathrm{sh}} \leqslant 40$). The largest decomposed matrix (for the irrep F_2) has the size 1650 among 12341 single-particle bases in total.

APPENDIX C: A SIMPLE WAY OF CALCULATING MASLOV INDICES FOR ISOLATED PERIODIC ORBITS IN THREE DIMENSIONS

The Maslov index σ_{po} for a periodic orbit (PO) is practically obtained as the sum of two contributions [12,13]. One is from the number of conjugate points μ_{po}, singularities of the semiclassical propagator, and the other is the number of negative eigenvalues ν_{po} of the matrix

$$\left(\frac{\partial^2 S(\mathbf{r}'',\mathbf{r}')}{\partial \mathbf{r}'' \partial \mathbf{r}''} + \frac{\partial^2 S(\mathbf{r}'',\mathbf{r}')}{\partial \mathbf{r}'' \partial \mathbf{r}'} + \frac{\partial^2 S(\mathbf{r}'',\mathbf{r}')}{\partial \mathbf{r}' \partial \mathbf{r}''} + \frac{\partial^2 S(\mathbf{r}'',\mathbf{r}')}{\partial \mathbf{r}' \partial \mathbf{r}'} \right)_{po}, \tag{C1}$$

which arises when one evaluates the trace integral by means of a stationary phase approximation. Here, S is the action integral along the PO

$$S(\mathbf{r}'',\mathbf{r}') = \int_{\mathbf{r}'}^{\mathbf{r}''} \mathbf{p} \cdot d\mathbf{r}, \tag{C2}$$

and $\mathbf{r}'' = \mathbf{r}'$ is an arbitrary point on the orbit. Each of those two contributions (μ_{po} and ν_{po}) depends on the choice of the initial point $\mathbf{r}'$ or the choice of coordinate set, but the sum $\sigma_{po} = \mu_{po} + \nu_{po}$ does not depend on such conditions. The matrix (C1) is directly connected to the monodromy matrix [12] and there are no difficulties in obtaining ν_{po}. Let us consider the way of counting conjugate points with respect to initial point $\mathbf{r}'$. Conjugate points are classified into three kinds of singularities: turning points, focal points, and caustics. At the turning point, the velocity becomes zero and the orbit forms a cusp there. At the focal points, a group of orbits ejected from initial point $\mathbf{r}'$ with momentum directions slightly deviated from $\mathbf{p}'$ concentrates into the original orbit with respect to one direction. At caustics, the orbit contacts with the envelope formed by the above group of orbits. The focal points and caustics along the orbits correspond to the singularities of the determinant

$$\det\left(-\frac{\partial^2 S(\mathbf{r},\mathbf{r}')}{\partial \mathbf{r} \partial \mathbf{r}'} \right)_{2,3} = \det\left(\frac{\partial \mathbf{p}'}{\partial \mathbf{r}} \right)_{2,3}, \tag{C3}$$

namely the zeros of the determinant

$$\det\left(\frac{\partial \mathbf{r}}{\partial \mathbf{p}'} \right)_{2,3} \equiv \det(D)_{2,3}. \tag{C4}$$

The suffixes imply the local Cartesian coordinates where the first axis is taken along the PO and the second and third axes
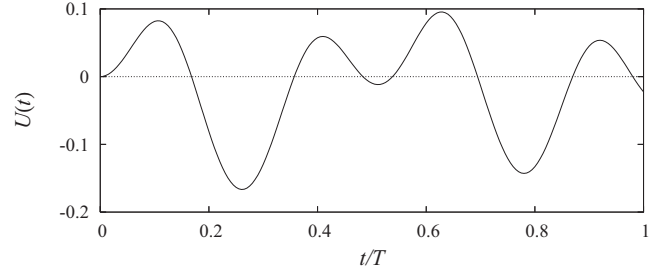

FIG. 9. The function $U(t)$ of Eq. (C9), calculated for one of the orbits TB with $\alpha = 6.0$ and $\beta_{td} = 0.1$.

are perpendicular to it. Let us consider two orbits in the vicinity of the PO, whose initial momentum $\mathbf{p}'$ is infinitesimally shifted towards the second and third axes, respectively, by

$$\delta\mathbf{p}'_2 = \begin{pmatrix} 0 \\ \eta_2 \\ 0 \end{pmatrix}, \quad \delta\mathbf{p}'_3 = \begin{pmatrix} 0 \\ 0 \\ \eta_3 \end{pmatrix}. \tag{C5}$$

Then, the deviations of those orbits from PO are

$$\delta\mathbf{r}_2 = \left(\frac{\partial \mathbf{r}}{\partial \mathbf{p}'} \right) \delta\mathbf{p}'_2 = \begin{pmatrix} D_{12} \\ D_{22} \\ D_{32} \end{pmatrix} \eta_2, \tag{C6}$$

$$\delta\mathbf{r}_3 = \left(\frac{\partial \mathbf{r}}{\partial \mathbf{p}'} \right) \delta\mathbf{p}'_3 = \begin{pmatrix} D_{13} \\ D_{23} \\ D_{33} \end{pmatrix} \eta_3, \tag{C7}$$

and one has

$$(\det D)_{2,3} = D_{22}D_{33} - D_{23}D_{32} = \frac{1}{\eta_2\eta_3}(\delta\mathbf{r}_2 \times \delta\mathbf{r}_3)_1. \tag{C8}$$

Together with turning points $|\dot{\mathbf{r}}| = 0$, the total number of conjugate points is obtained by counting the zeros of the quantity

$$U(t) = \frac{1}{|\delta\mathbf{p}'_2||\delta\mathbf{p}'_3|}(\delta\mathbf{r}_2(t) \times \delta\mathbf{r}_3(t)) \cdot \dot{\mathbf{r}}(t) \tag{C9}$$

along PO ($0 < t < T_{po}$). Figure 9 shows an example of $U(t)$ for three-dimensional orbit TB with $\alpha = 6.0$ and $\beta_{td} = 0.1$. One obtains $\mu = 7$ from this plot.

[1] S. Takami, K. Yabana, and M. Matsuo, Phys. Lett. B **431**, 242 (1998).

[2] J. Dudek, A. Goźdź, N. Schunck, and M. Miśkiewicz, Phys. Rev. Lett. **88**, 252502 (2002), and references therein.

[3] S. Tagami, Y. R. Shimizu, and J. Dudek, Prog. Theor. Phys. Suppl. **196**, 334 (2012).

[4] I. Hamamoto, B. R. Mottelson, H. Xie, and X. Z. Zhang, Z. Phys. D **21**, 163 (1991).

[5] S. M. Reimann, M. Koskinen, H. Häkkinen, P. E. Lindelof, and M. Manninen, Phys. Rev. B **56**, 12147 (1997).

[6] K. Arita, Int. J. Mod. Phys. E **13**, 191 (2004).

[7] K.-i. Arita, Phys. Rev. C **86**, 034317 (2012).

[8] A. G. Magner, A. A. Vlasenko, and K. Arita, Phys. Rev. E **87**, 062916 (2013).

[9] L. D. Landau and E. M. Lifshiz, *Quantum Mechanics (Nonrelativistic Theory)* (Pergamon Press, New York, 1981).

[10] T. Inui, Y. Tanabe, and Y. Onodera, *Group Theory and Its Applications in Physics* (Springer-Verlag, Berlin, 1990).

[11] K.-i. Arita and M. Brack, Phys. Rev. E **77**, 056211 (2008).

[12] M. C. Gutzwilldr, J. Math. Phys. **8**, 1979 (1967); **12**, 343 (1971).

[13] M. Brack and R. K. Bhaduri, *Semiclassical Physics* (Addison Wesley, Reading, 1997).

[14] V. M. Strutinsky, Nucl. Phys. A **95**, 420 (1967); **122**, 1 (1968).

[15] V. M. Strutinsky, A. G. Magner, S. R. Ofengenden, and T. Døssing, Z. Phys. A **283**, 269 (1977).

[16] K. Arita and K. Matsuyanagi, Nucl. Phys. A **592**, 9 (1995).

[17] A. Sugita, K. Arita, and K. Matsuyanagi, Prog. Theor. Phys. **100**, 597 (1998).

[18] K. Arita, A. Sugita, and K. Matsuyanagi, Prog. Theor. Phys. **100**, 1223 (1998).

[19] A. G. Magner, S. N. Fedotkin, K. Arita, T. Misu, K. Matsuyanagi, T. Schachner, and M. Brack, Prog. Theor. Phys. **102**, 551 (1999).

[20] A. G. Magner, K. Arita, and S. N. Fedotkin, Prog. Theor. Phys. **108**, 853 (2002).

[21] K. Arita and M. Brack, J. Phys. A: Math. Theor. **41**, 385207 (2008).

[22] W. Nazarewicz and J. Dobaczewski, Phys. Rev. Lett. **68**, 154 (1992).

[23] A. M. Ozorio de Armeida, *Hamiltonian Systems: Chaos and Quantization* (Cambridge University Press, Cambridge, 1988); A. M. Ozorio de Armeida and J. H. Hanney, J. Phys. A **20**, 5873 (1987).

[24] M. Baranger, K. T. R. Davies, and J. H. Mahoney, Ann. Phys. (NY) **186**, 95 (1988).

[25] D. Provost, Phys. Rev. E **51**, 5396 (1995).

[26] H. Schomerus and M. Sieber, J. Phys. A: Math. Gen. **30**, 4537 (1997).